Structure and energetics of Xe_n^-

Glenn J. Martyna and Bruce J. Berne
Department of Chemistry, Columbia University, New York, New York 10027

(Received 30 October 1987; accepted 2 December 1987)

Diffusion Monte Carlo simulations were performed to determine the absolute binding energies of an excess electron to small clusters of xenon atoms ($n \leqslant 19$). It was found that clusters as small as Xe_6 could bind the electron. The ground state wave function of the excess electron and the decomposition of the binding energy of the electron into kinetic and potential parts were determined for a number of small clusters. Large ($n > 50$) and small clusters anions were then studied at finite temperatures using path integral Monte Carlo. In all cases the excess electron in small clusters was found to exist in very diffuse state extending well beyond the radius of the cluster. However, in large clusters the electron was localized within the bulk of the cluster. Various properties are presented to characterize the electron in Xe_n^- as function of cluster size and the results compared to an electron solvated in fluid xenon.

I. INTRODUCTION

The attachment of an excess electron to neutral clusters of atoms or molecules has been the subject of much experimental interest.[1-3] However, as a detailed microscopic picture of an excess electron in a cluster has not emerged from this work, there are many questions about the formation of cluster anions that remain unanswered. For example, what is the breakup of the electronic binding energy into potential energy and kinetic energy and what is the spatial distribution of the excess electron? It is unclear whether the electron probability distribution is concentrated in the bulk or on the surface of the cluster, or how the distribution changes as a function of cluster size. The attachment of an electron to a large cluster should be analogous to the solvation of an excess electron in bulk fluids—a topic of great current interest. What are the differences between electronic processes in clusters and bulk fluids? It has been shown that considerable rearrangement of the solvent can occur in certain electron-bulk systems.[4-6] This effect may or may not occur in the cluster anions.

Xenon cluster anions, Xe_n^-, are studied here. Though one xenon atom will not bind an electron, xenon is very polarizable and it is therefore reasonable to assume that an electron will attach to Xe_n when n is large enough. Since accurate potential energy functions are known for both the xenon–xenon and the electron–xenon interaction, this is an ideal system to study. Also, comparisons may be made to the bulk system studied by Coker *et al.*[4]

Diffusion Monte Carlo simulations were performed to determine the binding (ground state) energy and structure of an electron in small clusters of xenon atoms ($n < 19$) frozen in the minimum energy geometries described by Hoare and Pal[7,8]. Clusters as small as Xe_6 were found to bind an excess electron. The electron was found to exist in a diffuse state in these small clusters. The results of the ground state calculations for Xe_{13}^- were compared to low temperature path integral Monte Carlo (PIMC) calculations (10 K) and found to be in good agreement. The restriction to frozen xenon atoms was then relaxed and both large and small clusters were studied at higher temperatures (50 K $n = 13$, 50, 100 and 100 K $n = 100$). In the large clusters the electron was almost entirely solvated and its properties resembled those on an electron in a bulk fluid.

II. METHODOLOGY

Two methods were used to simulate the Xe_n^- anions: diffusion Monte Carlo and path integral Monte Carlo.

A. Diffusion Monte Carlo

Diffusion Monte Carlo developed by Storer and Anderson,[9-11] offers a powerful method for treating ground state problems and has been applied to many interesting systems. The method is based on solving the imaginary time Schrödinger equation. For an electron moving in a potential field of n frozen xenon atoms this equation is

$$\frac{\partial \psi(\mathbf{r},\tau)}{\partial \tau} = -H\psi(\mathbf{r},\tau) = \left\{\frac{\hbar^2}{2m_e}\nabla^2 - [V(\mathbf{r}) - V_{\text{ref}}]\right\}\psi(\mathbf{r},\tau), \quad (2.1)$$

where V_{ref} is a reference energy and $V(\mathbf{r})$ is assumed to be

$$V(\mathbf{r}) = \sum_{i=1}^{n} V_{e\text{-Xe}}(|\mathbf{r} - \mathbf{R}_i|). \quad (2.2)$$

Here $\mathbf{R}_i$ is the position of the ith xenon atom and $V_{e-\text{Xe}}$ is the electron–xenon pseudopotential.[4]

Equation (2.1) can be regarded as a diffusion equation modified by a first order chemical rate equation with a position dependent "rate constant" $V(\mathbf{r})$. If the time, τ, is subdivided into sufficiently small time intervals, $\Delta\tau$, over which the diffusion process and the birth death kinetics are independent, the full propagation can be regarded as the evolution of an ensemble whose members diffuse in space and are then replicated or destroyed. At long times, the ensemble will be distributed according to the ground state wavefunction, $\psi_0(\mathbf{r})$.[10] When the potential energy is a rapidly varying function of position, $\Delta\tau$ must be taken extemely small and the variance of calculated quantities will be large. This is an inefficient algorithm and can be improved by *importance sampling*.[12,13]

Schrödinger's equation can be transformed from an

 0021-9606/88/074516-10$02.10

equation for $\psi(\mathbf{r},\tau)$, the wave function, to an equation for $f(\mathbf{r},\tau)=\psi(\mathbf{r},\tau)\psi_T(\mathbf{r})$, where ψ_T is an arbitrary function of the electron coordinates:

$$\frac{\partial f(\mathbf{r},\tau)}{\partial\tau}=\frac{\hbar^2}{2m_e}\nabla^2 f(\mathbf{r},\tau)-\frac{\hbar^2}{m_e}\nabla[f(\mathbf{r},\tau)\cdot\nabla\log\psi_T(\mathbf{r})] - \left[\frac{H\psi_T(\mathbf{r})}{\psi_T(\mathbf{r})}-V_{\text{ref}}\right]f(\mathbf{r},\tau). \tag{2.3}$$

The familiar diffusion term and first order rate process term again appear. The position dependent rate constant is, however, $H\psi_T/\psi_T$. If ψ_T is chosen to closely resemble an eigenfunction of H, the rate constant will be a slowly varying function of position. Thus, $\Delta\tau$ can be taken larger and variances are much smaller than was the case before the introduction of importance sampling. There is also an additional drift term [the second term on the right-hand side of Eq. (2.3)] whose effect is to push the ensemble members away from unfavorable regions of configuration space.

A good choice of $\psi_T(\mathbf{r})$ leads to the rapid convergence of the algorithm. A pair product form was chosen because it is both inexpensive to calculate and a reasonable approximation to the ground state wave function. The idea is to take two-body correlations into account directly while treating many-body correlations effectively. This form has often been used in variational calculations, the most notable example of which is liquid ^{4}He[14,15]:

$$\psi_T(\mathbf{r})=\prod_{i=1}^{n}h(|\mathbf{r}-\mathbf{R}_i|). \tag{2.4}$$

Two different functional forms for $h(r)$ were used in the present calculations. The first is the zero energy s-wave solution to the Schrödinger equation for the interaction of an electron with a single xenon atom[16]:

$$\left[\frac{\hbar^2}{2m_e}\nabla^2-V_{e\text{-Xe}}(r)\right]rh_1(r)=0. \tag{2.5}$$

$h_1(r)$ was chosen because it has no variational parameters. The variational principle

$$E_0\leqslant\frac{\int\phi^*H\phi}{\int\phi^*\phi} \tag{2.6}$$

is meaningful only for bound state problems. Thus, simulations based on Eq. (2.3) using $h_1(r)$ as the importance sampling function, were performed to detemine the set of clusters that would bind the electron. Having determined which electron–cluster systems were bound, variational calculations were performed on these systems using a second function

$$h_2(r)=\exp\left[\frac{\gamma r}{r(r^3+c)}-\alpha r\right]. \tag{2.7}$$

This form was chosen in order to accurately represent both the short and long range behavior of ψ_0. Since h_1 seemed to be a reasonable approximation to ψ_0 at small r, the parameters γ and c were fit to the rise of $h_1(\mathbf{r})$. The long range behavior obtained from simulations using h_1 suggested an exponential form for the fall off at large r. The constant α determining the rate of the fall off was variationally adjusted. The variational integrals were evaluated numerically using a three dimensional quadrature.[17] The resulting ψ_T was sufficiently close to the ground state wave function that potential and kinetic energy and structure could be calculated using the interpolation formula[13]:

$$\langle A\rangle_{\psi^2}\cong 2\langle A\rangle_f-\langle A\rangle_{\psi_T^2}. \tag{2.8}$$

The virial estimator was used to calculate the kinetic energy in all cases. The total energy E_0 can be calculated by averaging $H\psi_T/\psi_T$:

$$\left\langle\frac{H\psi_T}{\psi_T}\right\rangle_f=\frac{\int\psi_0\psi_T(H\psi_T)/\psi_T dv}{\int f dv} =\frac{\int\psi_T H\psi_0 dv}{\int f dv}=E_0. \tag{2.9}$$

The cluster geometries used in the calculations were those determined by Hoare and Pal. The exact lowest energy geometries were used for $n=7$, 13, otherwise the geometries used by Hoare and Pal at the start of their minimization procedure were taken.[7,8]

Simulations of Eq. (2.3) using h_1 were run for 20 000 time steps and averages were collected for 10 000 time steps ($\Delta T=0.68$). Simulations using h_2 were run for 60 000 time steps and averages were collected for 50 000 time steps ($\Delta T=0.17$).

B. Path integral Monte Carlo

The density matrix in the position representation can be expressed as

$$\rho(\mathbf{r},\mathbf{r}';\beta) =\int d\mathbf{r}^1\cdots d\mathbf{r}^{P-1}\prod_{i=0}^{P}\rho\left(\mathbf{r}^i,\mathbf{r}^{i+1};\frac{\beta}{P}\right), \tag{2.10}$$

$$\rho\left(\mathbf{r},\mathbf{r}';\frac{\beta}{P}\right)=\langle\mathbf{r}|e^{-\beta H/P}|\mathbf{r}'\rangle, \tag{2.11}$$

where $\mathbf{r}^1$ equals $\mathbf{r}$ and $\mathbf{r}^{P+1}$ equals $\mathbf{r}'$. The Hamiltonian for the electron–cluster system is

$$H=\frac{-\hbar^2}{2m_e}\nabla^2+\sum_{i=1}^{n}V_{e\text{-Xe}}(|\mathbf{r}-\mathbf{R}_i|) \times\frac{-\hbar^2}{2m_{\text{Xe}}}\sum_{i=1}^{n}\nabla_i^2+\sum_{i>j=1}^{n}V_{\text{Xe-Xe}}(|\mathbf{R}_i-\mathbf{R}_j|), \tag{2.12}$$

where $V_{\text{Xe-Xe}}$ is the Lennard-Jones potential ($\sigma=4.0551$ Å and $\epsilon=229$ K). If P is taken sufficiently large, the primitive high temperature approximation to the density matrix may be substituted into Eq. (2.10).[18–23] The diagonal elements of the resulting density matrix may be then simplified to yield

$$\rho(\mathbf{r},\mathbf{R};\mathbf{r}\mathbf{R})=\int d\mathbf{r}^1\cdots\int d\mathbf{r}^{P-1}\int d\mathbf{R}^1\cdots\int d\mathbf{R}^n \times\exp\left[-\beta\sum_{i>j=1}^{n}V_{\text{Xe-Xe}}(|\mathbf{R}_i-\mathbf{R}_j|)\right] \times\exp\left[-\frac{m_e P}{2\hbar^2\beta}\sum_{i=1}^{P}(\mathbf{r}_i-\mathbf{r}_{i+1})^2 -\frac{\beta}{P}\sum_{i=1}^{P}\sum_{j=1}^{n}V_{e\text{-Xe}}(|\mathbf{r}_i-\mathbf{R}_j|)\right], \tag{2.13}$$

where because $\hbar^2\beta/m_{\text{Xe}}$ is extremely small, the xenon atoms are described classically. This formulation of the density ma-

trix is isomorphic to a classical cyclic chain polymer in a bath of xenon atoms. All equilibrium properties and imaginary time correlation functions can be calculated by taking the appropriate traces over the density matrix:

$$\langle A \rangle = \frac{\mathrm{Tr}\,\rho A}{\mathrm{Tr}\,\rho}. \tag{2.14}$$

In order to describe an electron in low temperature clusters, it is necessary to treat very large polymer chains ($P \sim 10^5$). Therefore the force constants of the harmonic bonds of the polymer are extremely large ($k = m_e P/2\hbar^2\beta$). Ordinary metropolis Monte Carlo or molecular dynamics algorithms, which make no special provisions to treat these harmonic degrees of freedom, take a prohibitively long time to converge because only very small amplitude moves of these degrees of freedom are accepted.[23–26] To treat this problem, efficient methods first used in force bias[27] and smart Monte Carlo[28] are required.

The metropolis Monte Carlo[29] algorithm generates a Markov process with a transition probability distribution, $W(X,X')$, chosen so that after some equilibration time, the configurations are distributed according to $P(X) = \exp[-S(X)]/Q$ where $S(X)$ is the Euclidean action, and Q is the partition function. $W(X,X')$ is

$$W(X,X') = T(X',X)\min\left[1, \frac{T(X,X')P(X')}{T(X',X)P(X)}\right], \tag{2.15}$$

where $T(X,X')$ is a conditional probability distribution function from which particle moves are sampled. The beads of the polymer chain representing the electron were sampled from

$$T(r_0,r_{j+1}) = \prod_{k=1}^{j}\left(\frac{1}{2\pi\sigma_k^2}\right)\exp\left(-\frac{(r_k - r_k^*)^2}{2\sigma_k^2}\right), \tag{2.16}$$

$$r_k^* = \frac{(j+1-k)r_{k-1} + r_{j+1}}{(j+2-k)}, \tag{2.17}$$

$$\sigma_k^2 = \frac{2\beta\hbar^2(j+1-k)}{Pm_e(j+2-k)}, \tag{2.18}$$

where j is the number of beads on the section of chain to be moved and r_0 and r_{j+1} are the end points of the section. This efficient choice of $T(r,r')$ for the polymer was first pointed out by Ceperley.[25] It is exact for a quantum mechanical free particle, a system that only contains harmonic bonds. Thus, the harmonic bonds of the polymer are in some sense eliminated from the problem. The algorithm for moving the electronic coordinates is to slice out and replace sections of chain between fixed end points. The sections are chosen large enough that the acceptance probability of the many particle move is around 50%. One staging pass is thus defined as P (the total number of beads) moves of the chosen section length. This algorithm is discussed elsewhere in more detail.[4]

Path integral Monte Carlo simulations on Xe_{13}^- at 50 K were performed using $P = 8000$ total beads moving section lengths of $j = 400$ beads for 100 staging passes. Xe_{100}^- and Xe_{50}^- at 50 K were simulated using $P = 4000$ beads moving section lengths of $j = 25$ beads for 400 staging passes while Xe_{100}^- at 100 K was simulated using $P = 2000$ beads moving section lengths of $j = 25$ beads for 400 staging passes. The xenon atoms in all cases were simulated for $j \cdot S_p$ standard Monte Carlo passes where S_p is the number of staging passes.

III. RESULTS

A. Diffusion Monte Carlo simulations of Xe_n^-

Diffusion Monte Carlo simulations utilizing the importance sampling function h_1, gave extremely precise and accurate binding energies, $|E_0|$, for the excess electron. The smallest cluster studied was Xe_6^- and the binding energy of the excess electron was found to be 12 K. Clusters smaller than 6 were not studied because the intrinsic accuracy of our methods cannot establish whether or not they are bound though 12 K can be taken as an upper bound on their binding energies. In Fig. 1 the ground state energies for Xe_6^- through Xe_{19}^- are plotted vs cluster size and in Fig. 2 the cluster geometries used in the simulation are presented. The binding

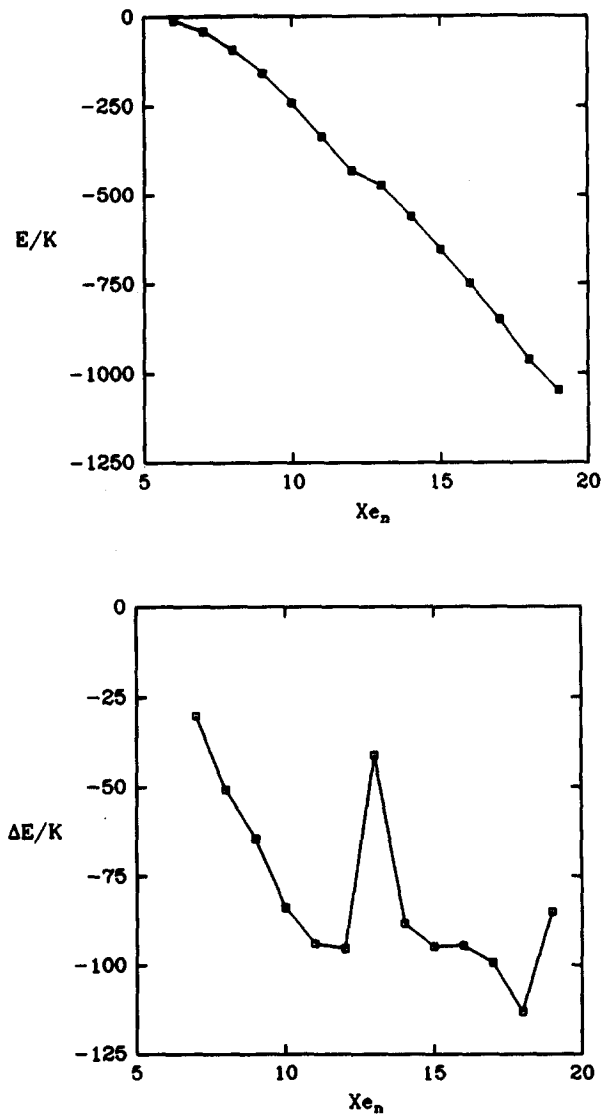

FIG. 1. Top: The ground state energy of an excess electron in Xe_n as a function of cluster size n. Bottom: The difference between the ground state energy of an excess electron in Xe_n and Xe_{n+1} as a function of cluster size.

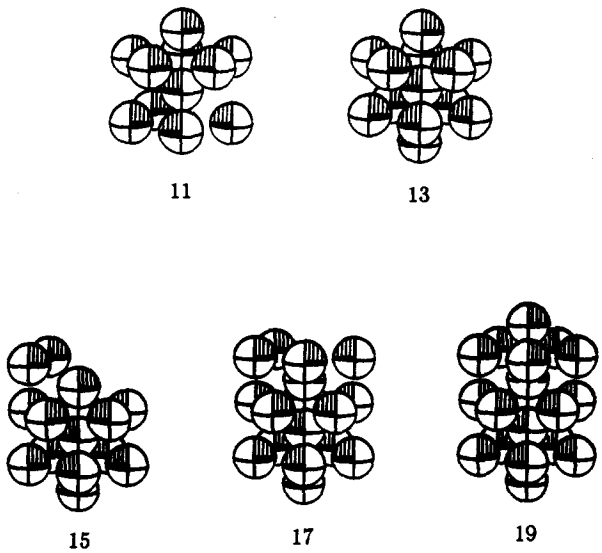

FIG. 2. Lowest energy geometries of Xe_{11}, Xe_{13}, Xe_{15}, Xe_{17}, and Xe_{19}.

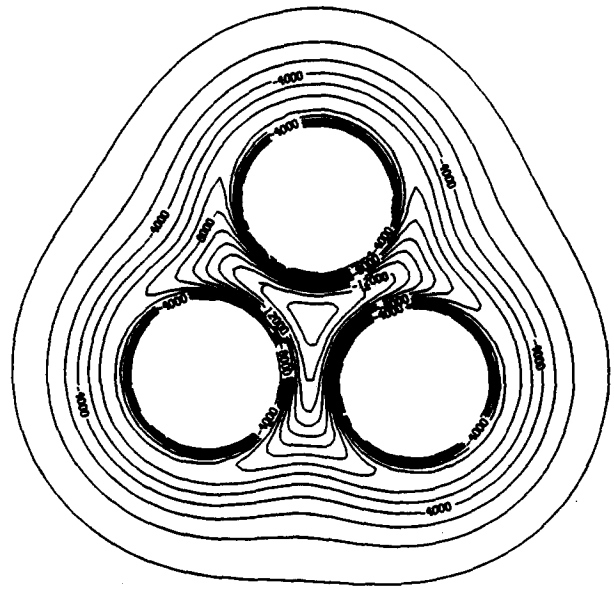

FIG. 4. The potential energy surface ($z = 0$) of Xe_3^-. (Energy in Kelvin; contour interval is -1000 K.)

energy $|E_0|$ increases monotonically with cluster size [see Fig. 1(b) the first derivative of Fig. 1].

The microscopic details of this result can be elucidated by examining the electron–xenon pseudopotential (Fig. 3) and the positions of the xenon atoms in the clusters. The potential energy is large and positive near $r_{e\text{-}Xe} \sim 0$ and has a deep minimum, 6000 K, at $r_{e\text{-}Xe} \sim d_{\min}/2$ where $d_{\min}$ is the minimum of the xenon–xenon potential. Therefore, when two xenon atoms are placed $d_{\min}$ apart the minima of the pair wise electron–xenon pseudopotential roughly overlap. This forms a channel of negative potential energy between two sources of large positive potential energy. The regions of negative potential energy outside the two atoms can be thought of as open channels. In Fig. 4 the channels are illustrated for Xe_3. A broad, shallow, open channel can be seen surrounding the cluster while the interior of the cluster contains deeper but narrower channels. Larger clusters, of course, possess similar channels. Upon the addition of a xenon atom to a cluster, existing channels are extended and new channels are created. Since the channels form the basis for electron attachment the binding energy increases with cluster size. However, the binding energy increases more slowly between $n = 12$ and $n = 13$. This occurs because the lowest energy cluster geometry undergoes a significant transformation at this size. Upon adding the thirteenth atom to the apex of Xe_{12} the cluster contracts into an icosohedron Xe_{13} (Fig. 2). All channels in the interior of the cluster then narrow and the open channels at the apex are closed. Note that the same sort of decreased rise of the binding energy occurs between Xe_{18}^- and Xe_{19}^- when again the open channels at the apex of the cluster are closed. This shrinkage of the channels causes the change in kinetic energy to increase relative to the change in potential energy, thus slowing the rise of the binding energy. The interplay between kinetic energy and potential energy is therefore a crucial mechanism in electron attachment.

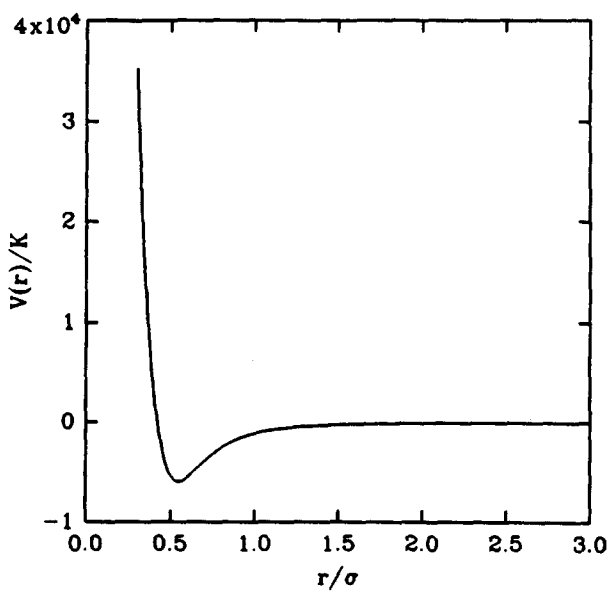

FIG. 3. The electron–xenon psuedopotential as a function of separation measure in xenon atom diameters.

In order to determine the spatial distribution of the elecron and the breakup of the binding energy into potential and kinetic parts, a more accurate importance sampling function was required. Therefore variational calculations were performed on h_2 as discussed in Sec. II. Optimized average energies were found to be within about 20% of the values found from simulations using h_1, for clusters Xe_n, $n > 10$. These energies and the values of the variational parameter α are summarized in Table I. Diffusion Monte Carlo simulations performed using the optimized h_2 as an importance sampling function to obtain the desired data.

The basic structure of the electron is described by the electron-cluster center of mass $P(r)$, the electron probability distribution at a distance r from the center of mass of the cluster. This function is shown in Fig. 5 for a number of clusters. The vertical line in Fig. 5 represents the center of

TABLE I. Variational calculations.

Cluster	E_{exact}/K	$\langle E\rangle$/K	α(a.u.)
Xe_{11}^-	-335 ± 4	-275	0.0075
Xe_{12}^-	-430 ± 8	-349	0.007
Xe_{13}^-	-474 ± 8	-400	0.007
Xe_{14}^-	-559 ± 8	-478	0.007
Xe_{15}^-	-654 ± 8	-560	0.007
Xe_{16}^-	-748 ± 8	-642	0.0065
Xe_{17}^-	-847 ± 10	-731	0.0065
Xe_{18}^-	-960 ± 10	-825	0.007
Xe_{19}^-	-1046 ± 10	-900	0.0065

the xenon atom furthest from the center of mass of the largest cluster ($n=19$). Clearly, most of electron density is found outside the cluster. For example the probability of the electron being inside the cluster is 14% for Xe_{13}^- and approximately 20% for Xe_{19}^-. These estimates were obtained by intergrating the $P(r)$ up to the position of the furthest xenon atom from the center of mass of the cluster. The differences in behavior at short r in the $P(r)$ are caused by the varying proximity of a xenon atom to the center of mass of the cluster (see Fig. 2). The effect of the channels on the electron spatial distribution can be seen in the electron–xenon radial distribution function $g(r)$. This quantity is defined as the electron density a distance r from a xenon atom averaged over all xenon atoms (see Fig. 6) [$\int 4\pi r^2 g(r) = n$, the number of xenon atoms]. The first peak occurs at approximately $d_{min}/2$ and a second peak occurs at $3d_{min}/2$ thus denoting the position of the channels. As cluster size increases the first peak increases in height and the second peak sharpens. The sharpening of the first peak with cluster size indicates that the electron has a higher probability of being near a xenon atom in larger clusters. Note this is true even if the $g(r)$ are divided by n. Therefore, there is an indication that the electron is becoming more tightly bound to the cluster.

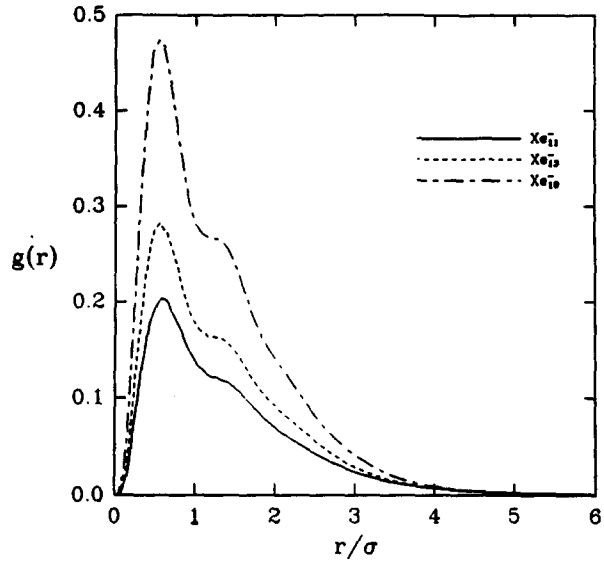

FIG. 6. The electron–xenon pair correlation functions $g(r)$ for three cluster sizes, $n=11, 13, 19$.

The breakup of the electron binding energy into its potential and kinetic parts (Fig. 7) supports the conclusion that the competition between kinetic energy and potential energy plays a crucial role in electron attachment. The basic trend is an increase of kinetic energy and a decrease of potential energy with cluster size. Again, this occurs because the addition of a xenon atom to a cluster increases the number and depth of the channels of negative potential energy. These sources of negative potential energy draw electron density into the narrow channel regions. This costs kinetic energy and the kinetic energy increases with cluster size. However, as electron density is concentrated in deeper and more numerous channels the potential energy of the electron decreases faster than the increase in kinetic energy. Therefore, the binding energy of the excess electron increases as the number of xenon atoms in the cluster increases. The breakup

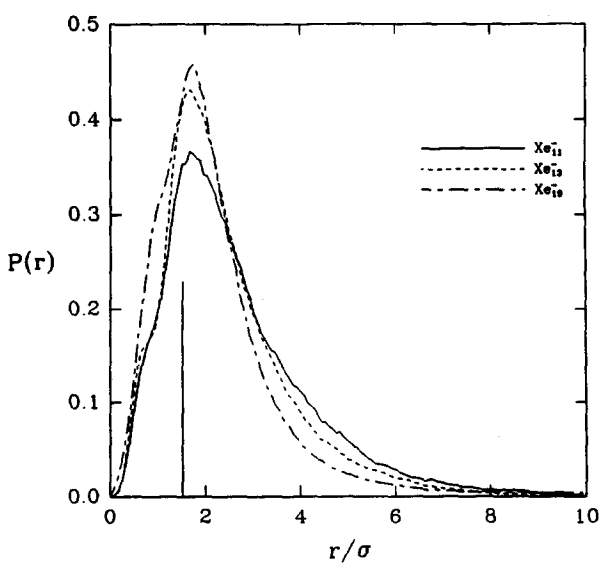

FIG. 5. The electron probability distribution with respect to the cluster center of mass $P(r)$ for three cluster sizes, $n=11, 13, 19$. The vertical line is the position of the furthest atom from the center of mass of Xe_{19}^-.

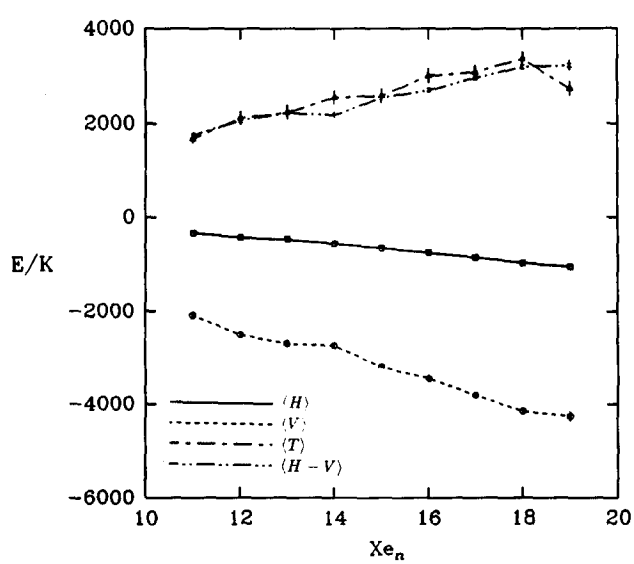

FIG. 7. The potential, kinetic, and total energies of an excess electron as a function of cluster size.

was not obtained accurately enough to completely verify the conclusions of the previous discussion about the decreased rise of the binding energy at $n = 12, 13$ and $n = 18, 19$. However, the general trends support the argument.

The only major assumption inherent in this work has been that the electron will not perturb the cluster ground state geometry from its neutral form. There are two reasons to expect this to be the case. The binding energy of the electron per xenon atom is small compared to the pure cluster binding energy per xenon atom. Also, the electron is spatially diffuse, tending to diminishe any perturbative effects. In order to test this assumption more thoroughly, a path integral calculation on Xe_{13}^- was performed at 50 K and no perturbations of the xenon structure were found.

As the above calculations were time consuming, it might be thought that a variation of the split operator FFT method[30] would be applicable to the electron–cluster system. The usual method is to propagate a wave function ψ in real time on a grid. Time correlation functions are generated which can be spectrally analyzed to determine eigenfunctions and eigenenergies. Inspired by diffusion Monte Carlo, an initial wave function was propagated in imaginary time and the value of an energy offset, V_{ref}, was adjusted to preserve the amplitude of the wave function. This procedure insures that $\psi(t_\infty)$ will be the ground state wave function and V_{ref} will be the ground state energy. In order to accurately represent the ground state wave function, we have devised an FFT method based on a spherical grid, equally spaced in the radial coordinate studies of the ground and excited states of cluster anions based on this FFT method will be presented in a separate paper.

B. Path integral Monte Carlo

In order to assess the accuracy of path integral Monte Carlo simulations of cluster systems, a test study was done on Xe_{13}^- with the xenon atoms frozen in their lowest energy geometry. The path integral was evaluated at $T = 10$ K for a number of different discretizations (P) and the results compared to the ground state (see Figs. 8 and 9). Figure 8 shows the convergence of the electron–xenon $g(r)$. For reference, the xenon–xenon radial distribution function, is shown below the electron–xenon $g(r)$ though it is not drawn to scale. Figure 9 graphically presents the convergence of the average potential energy and the average kinetic energy. The agreement of the path integral and the ground state quantities is fairly good although it takes from $P = 60\,000$ to $P = 80\,000$ to achieve convergence.

Having established the accuracy of PIMC simulations on cluster systems, the restriction to frozen clusters was relaxed and the Xe_{13}^- was studied at 50 K. The positions of the xenon atoms are now sampled from Eq. (2.12). Thus the electron moves on a potential energy surface subject to thermal motion. Figure 10 presents a comparison between the structural properties of Xe_{13} ($T = 0$ K) and Xe_{13}^- ($T = 50$ K). The probability distribution, $P(r)$, of finding a xenon atom a distance r from the center of mass of the cluster, and the xenon–xenon $g(r)$ shown in the figure illustrate that the cluster has undergone a considerable expansion. The previously discussed channels are therefore broader. This reduces the kinetic energy penalty that the excess electron must pay to become localized within the cluster. This increased localization can be seen in Fig. 11, where a comparison of the electron–cluster c.m. $P(r)$ for the system at 50 and 0 K is given. [The xenon–xenon c.m. $P(r)$ for Xe_{13}^- at 50 K is included in the figure as a guide to gauge the increased localization though it is drawn to a different scale.] The electron has a higher probability of residing in the channels of attractive potential energy within the cluster at 50 K. The expansion of the cluster has not decreased the depth of the channels significantly. The potential energy of the excess electron is lower at 50 K than at 0 K because of the increased localization in the attractive channels. The corresponding kinetic energy of the excess electron increases only slightly from 0 to 50 K despite the increased localization (see Table II). Thus the binding energy of an excess electron at 50 K is roughly double the binding at 0 K (see Table II). That an electron

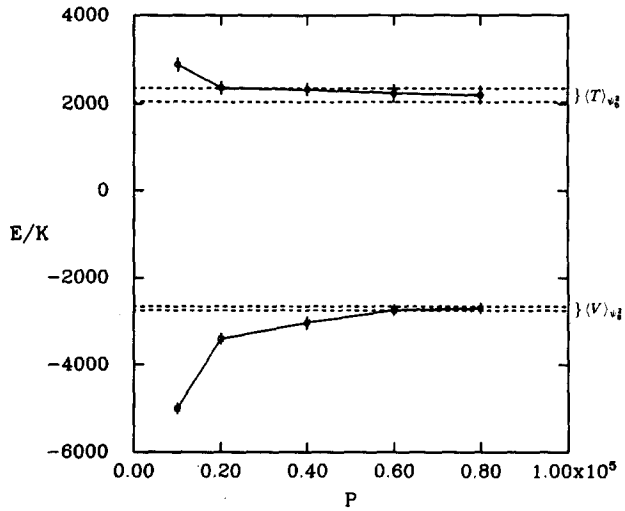

FIG. 8. The electron potential and kinetic energy as a function of discretization P for Xe_{13}^- at 10 K.

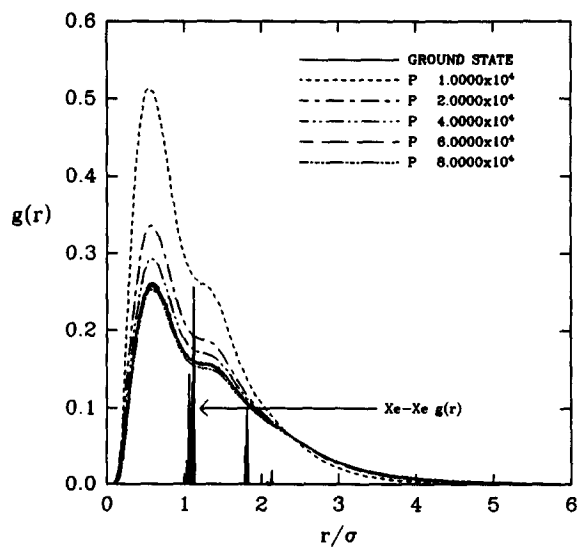

FIG. 9. The electron–xenon pair correlation functions $g(r)$ as a function of discretization P for Xe_{13}^- at 10 K. The xenon–xenon $g(r)$ is shown for reference and is not drawn to scale.

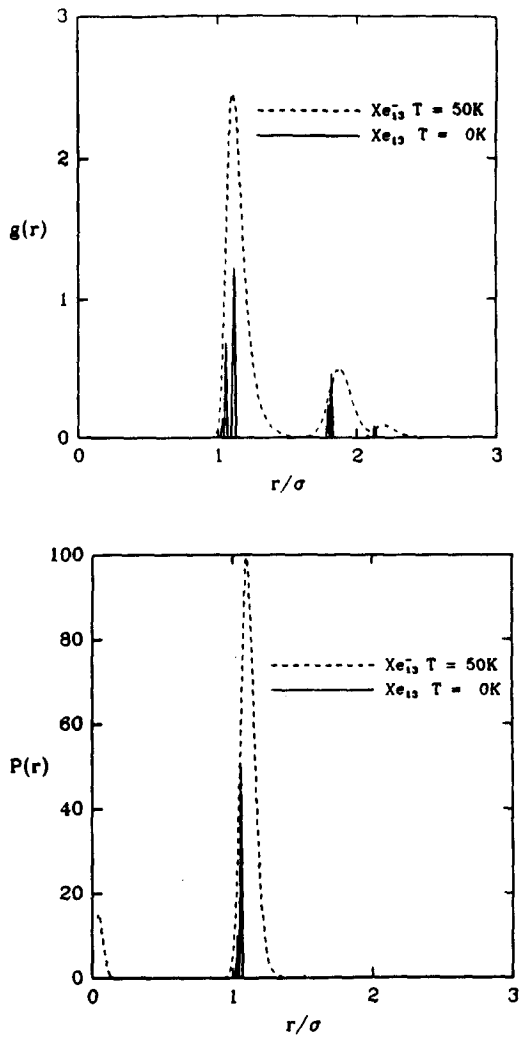

FIG. 10. Top: Comparison of the xenon–xenon pair correlation functions $g(r)$ for Xe_{13}^- at 50 and 0 K. The distribution at 0 K is not drawn to scale. Bottom: Comparison of the xenon probability distribution with respect to the center of mass $P(r)$ for Xe_{13}^- at 50 and 0 K. The distribution at 0 K is again not drawn to scale.

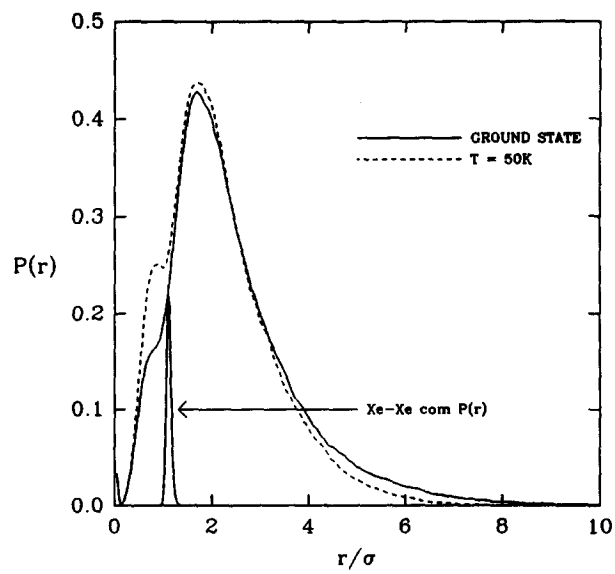

FIG. 11. Comparison of the electron probability distribution function with respect to the cluster center of mass $P(r)$ for Xe_{13}^- at 50 and 0 K. The xenon $P(r)$ at 50 K is shown for reference and is not drawn to scale.

can become more tightly bound at higher temperatures than at lower temperatures, is a rather counterintuitive result. It is however, nicely explained by the concept of channels. In spite of the increased binding, it should be noted that the electron density is still extremely diffuse and it does not perturb the xenon spatial distribution from its neutral form; the structure of Xe_{13}^- (Fig. 10) is indistinguishable from that of Xe_{13} at 50 K.

Small clusters can attach an electron. However, they cannot be said to solvate one. A large fraction of the electron density remains outside the cluster (see Fig. 5). Larger clusters, Xe_{50}^- and Xe_{100}^-, were therefore studied in the hope of observing solvation. Figure 12 gives the electron probability distribution with respect to the cluster center of mass superimposed upon the xenon probability distribution with respect to the cluster center of mass for Xe_{100}^- ($T = 50$ K and $T = 100$ K) and Xe_{50}^- ($T = 50$ K) anions. Clearly in the 100 atom cluster, the electron forms a bulk state; the electron is confined almost entirely within the cluster. The effective diameter of the excess electron has been reduced by a factor of 2 from its value in Xe_{13}^-. This has several effects on the properties of the excess electron. The kinetic energy increases dramatically from its value in smaller clusters. However, the potential energy decreases even more dramatically making solvation energetically favorable (see Table II). Again, the interplay between kinetic energy and potential energy was found to be a crucial element in electron attachment phenomena.

The best way to make contact with the fluid xenon simulation of Coker *et al.*, is to compare cluster properties with fluid properties at densities where the respective xenon–xenon $g(r)$ are similar. Thus both Xe_{50}^- and Xe_{100}^- at 50 K are roughly comparable to a fluid at a density of $\rho^* = 0.9$ (though a higher density would provide a better comparison) and Xe_{100}^- at 100 K is comparable to a fluid at a density of $\rho^* = 0.7$.[4] Of course, these comparisons are at best qualitative. The electron–xenon $g(r)s$ pictured in Fig. 13 show extremely well defined first and second peaks and the beginning of a third peak. [The xenon–xenon $g(r)$ is included in Fig. 13 as a reference though it is not drawn to scale.] The position and relative definition of the peaks is in good agreement with the fluid results.[4]

The spatial distribution of an excess electron in a cluster approaches that observed in the bulk fluid as cluster size is increased (see Fig. 14). The electron–xenon $g(r)$ should converge to fluid result in the large n limit but because the cluster systems are at a higher effective density and a lower temperature than the fluid system (simulated at 248 K) the peaks of the $g(r)$ are somewhat closer and sharper than

TABLE II. Average excess electron properties.

Cluster	Temp/K	$\langle V\rangle$/K	$\langle T\rangle$/K	$\langle E\rangle$/K
Xe_{13}^-	0	$-2\,698 \pm 50$	2200 ± 150	-474 ± 8
Xe_{13}^-	50	$-3\,400 \pm 100$	2400 ± 100	-1000 ± 140
Xe_{50}^-	50	$-12\,600 \pm 200$	6800 ± 500	-5800 ± 550
Xe_{100}^-	50	$-16\,100 \pm 200$	6500 ± 500	-9600 ± 550
Xe_{100}^-	100	$-14\,600 \pm 200$	5900 ± 500	-8700 ± 550

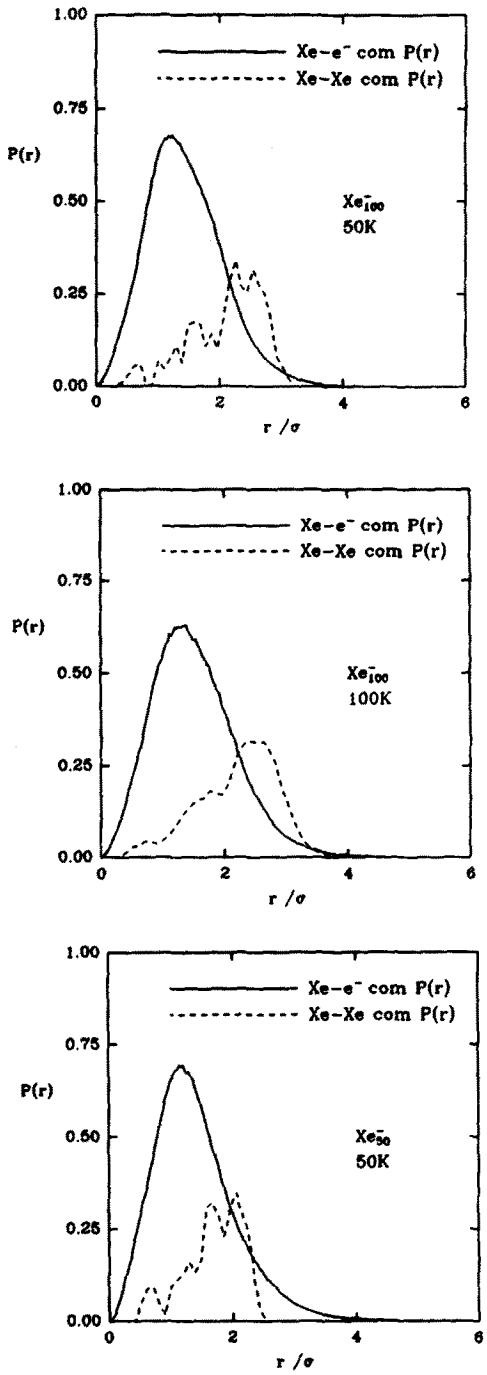

FIG. 12. The electron probability distribution with respect to the cluster center of mass $P(r)$ for an excess electron in the designated clusters. The xenon probability is shown as a reference and is not drawn to scale.

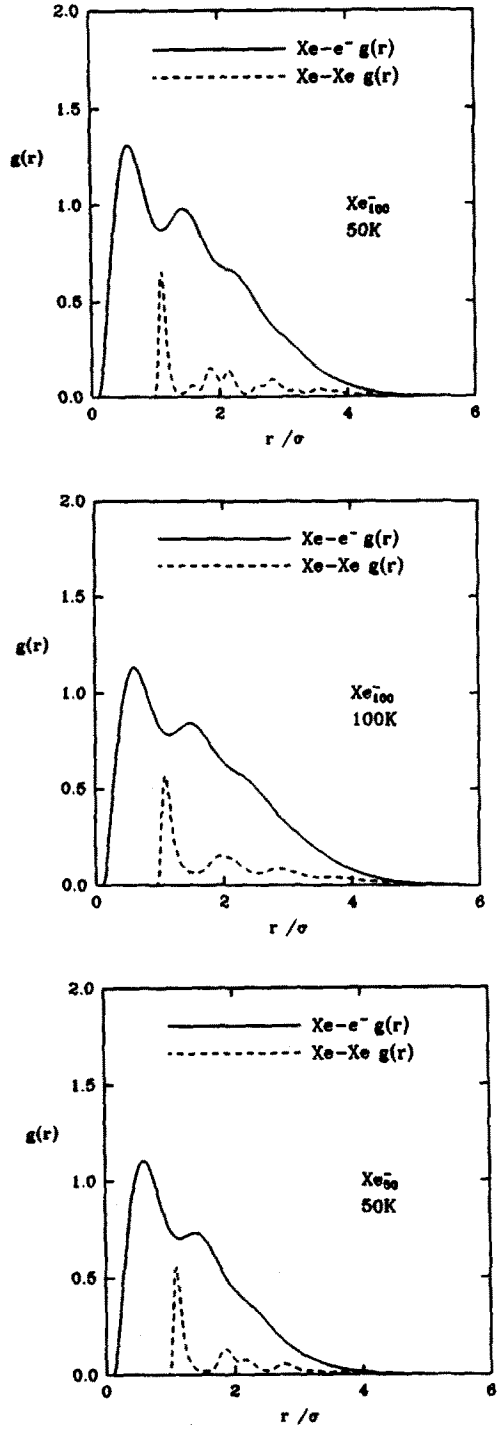

FIG. 13. The electron–xenon pair correlation function $g(r)$ for an excess electron in the designated clusters. The xenon–xenon pair correlation function $g(r)$ is shown as a reference and is not drawn to scale.

those in the bulk liquid. This is substantiated by trends in the fluid data[4] which indicate that an increase in density and a decrease in temperature will increase and shift to closer distances the peaks of the electron–xenon $g(r)$. Thus, cluster anions, Xe_n^-, resemble the fluid at large n.

The xenon–xenon radial distribution function of the Xe_{100}^- cluster changes from 50 to 100 K (Fig. 13). The cluster at 50 K is "solid-like" and at 100 K is "liquid-like". The electron–xenon correlation decreases as temperature increases (Fig. 13). This effect is also observed in the fluid.[4] The change from a solid-like to a liquid-like state involves two processes. Cluster "geometries" present in the solid are thermally broadened. Also new geometries not seen in the solid become accessible.[31] The thermal broadening and the new geometries allow nearest neighbor xenon atoms to sample configurations very far from the minimum of the Lennard-Jones potential with high probability. Since the channels are less structured, shallower and wider in the liquid-like cluster compared to the solid-like cluster the potential energy of the excess electron is higher in the liquid-

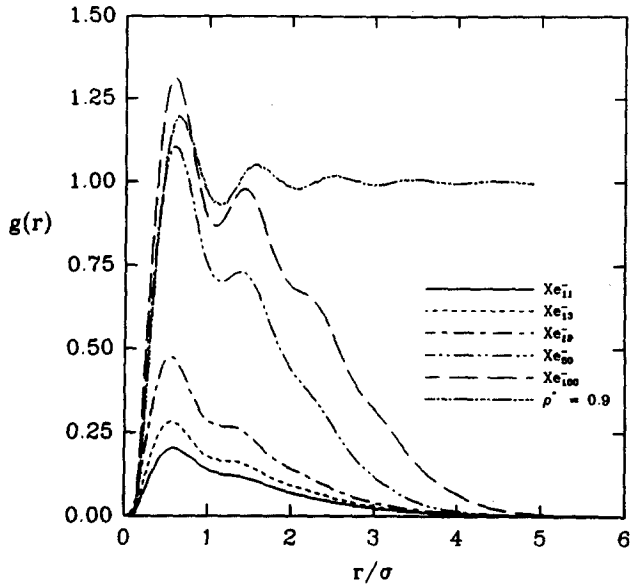

FIG. 14. The electron–xenon pair correlation function $g(r)$ for an excess electron in the designated clusters and for the fluid at $\rho^* = 0.9$.

like cluster. However, the kinetic energy of the excess electron is correspondingly reduced (see Table II). The resulting binding energy for Xe_{100}^- at 100 K is therefore 10% less than that of Xe_{100}^- at 50 K (see Table II).

In the low density subcritical fluid, the excess electron can strongly perturb the xenon structure. In regions around the electron the first peak of the $g(r)$ was sharpened relative to the pure fluid.[4] In contrast, the excess electron does not perturb the structure of small clusters. However, in Xe_{100}^- at 100 K, as liquid-like cluster, this same electrostriction is observed; the first peak in the xenon $g(r)$ is sharpened relative to that of the neutral species (see Fig. 15). Again, the excess electron has a minimum potential energy if neighboring xenon atoms are $d_{\min}/2$ apart. Therefore, the presence of an excess electron can reduce the thermal expansion of a cluster and cause a clustering to occur in a subcritical fluid. This will sharpen the first peak in the radial distribution function in both cases and also lower the xenon–xenon potential energy of the cluster from the neutral species (see Table III).

In the high density fluid the electron did not effect the xenon structure.[4] In the equivalent lower temperature clusters, Xe_{100}^- and Xe_{50}^-, there are negligible perturbations of the xenon–xenon $g(r)$ (see Fig. 15).

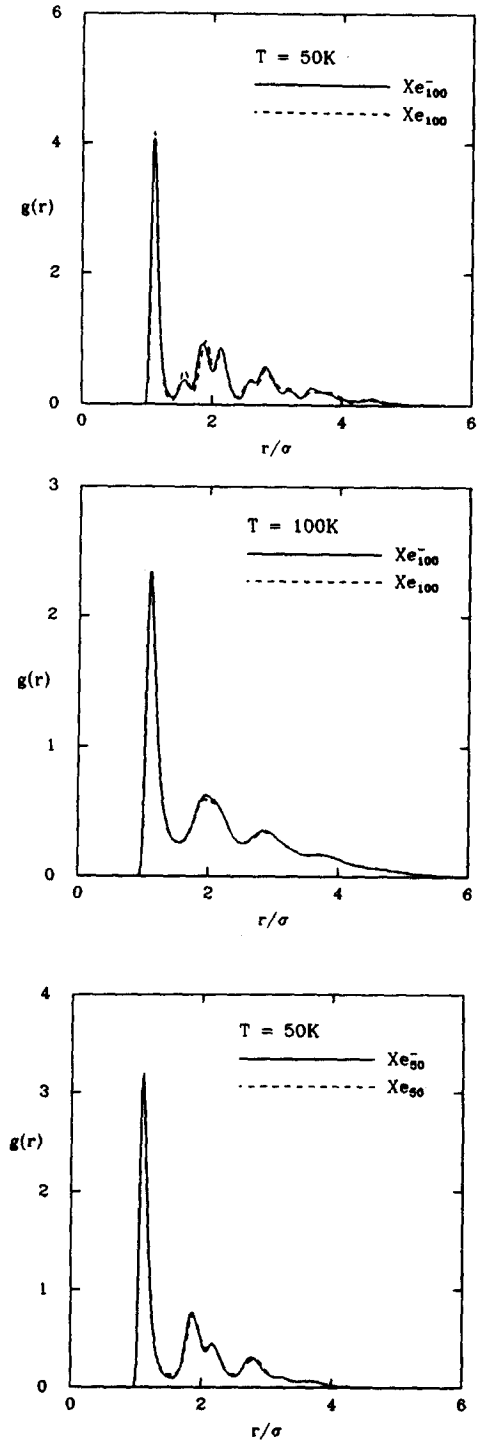

FIG. 15. Comparison of the xenon–xenon pair correlation functions $g(r)$ of the anions Xe_{100}^- and Xe_{50}^- and their corresponding neutral forms.

IV. DISCUSSION

The behavior of an excess electron in both small and large clusters has been studied. The electron was found to attach to small clusters $n>6$ where it exists in a diffuse state with a significant fraction of its density outside of the clusters. In larger clusters the electron forms a bulk state and its behavior is more like that of an electron solvated in a fluid. A simple picture based on attractive channels successfully explains the qualitative features of the observed structure and energetics of the electron–cluster systems.

A major assumption made in this work is the neglect of many body effects in the polarization of the xenon atoms.

TABLE III. Xenon–xenon potential energy.

Cluster	Temp/K	$\langle V_{Xe\text{-}Xe}\rangle/n$ K
Xe_{50}^-	50	-996 ± 3
Xe_{50}^-	50	-993 ± 3
Xe_{100}^-	50	-1165 ± 3
Xe_{100}^-	50	-1165 ± 3
Xe_{100}^-	100	-989 ± 3
Xe_{100}^-	100	-968 ± 3

The psuedopotential only includes two body polarization terms. Many body polarization should be included in a self-consistent approach because xenon is very polarizable. It remains to be seen if many body polarization will materially change the results presented in this paper. The effect will be investigated in a future publication.

ACKNOWLEDGMENTS

We would like to thank Professor David Coker for many useful discussions during the course of this work. This work was supported by a grant from NSF, and the simultions were run on a Convex C1 computer purchased with funds provided by an NSF departmental instrument grant.

[1]H. G. Schindler, H. Haberland, and D. R. Worsnop, Ber. Bunsenges Phys. Chem. **88**, 270 (1984).
[2]H. G. Schindler, H. Haberland, and D. R. Worsnop, J. Phys. Chem. **88**, 3903 (1984).
[3]M. Knapp, O. Echt, D. Kreisle, T. D. Mark, and E. Recknagel, Chem. Phys. Lett. **126**, 225 (1986).
[4]D. F. Coker, D. Thirumali, and B. J. Berne, J. Chem. Phys. **86**, 5689 (1987).
[5]A. Wallqvist, D. Thirumali, and B. J. Berne, J. Chem. Phys. **86**, 6404 (1987).
[6]J. Schnitker and P. J. Rossky, J. Chem. Phys. **86**, 3471 (1987).
[7]M. R. Hoare and P. Pal, Adv. Phys. **20**, 161 (1971).
[8]M. R. Hoare and P. Pal, Adv. Phys. **24**, 646 (1975).
[9]R. C. Grimm and R. G. Storer, J. Comp. Phys. **7**, 134 (1971).
[10]J. B. Anderson, J. Chem. Phys. **63**, 4121 (1975).
[11]J. B. Anderson, Int. J. Quantum Chem. **15**, 109 (1979).
[12]J. B. Anderson, J. Chem. Phys. **73**, 3897 (1980).
[13]D. M. Ceperley and B. J. Alder, Phys. Rev. Lett. **45**, 566 (1980).
[14]R. Jastrow, Phys. Rev. **98**, 442 (1955).
[15]W. L. McMillan, Phys. Rev. A **138**, 442 (1965).
[16]I. J. McGee and R. D. Murphy, J. Phys. C **5**, 311 (1972).
[17]D. J. Evans, Mol. Phys. **28**, 1233 (1974).
[18]R. P. Feynman, *Statistical Mechanics* (Benjamin, Reading, MA, 1972).
[19]L. D. Fosdick and H. F. Jordan, Phys. Rev. **143**, 58 (1966).
[20]J. A. Barker, J. Chem. Phys. **70**, 2914 (1978).
[21]D. C. Chandler, K. S. Schweizer, R. M. Stratt, and P. G. Wolynes, J. Chem. Phys. **75**, 1347 (1981).
[22]M. Herman, E. F. Bruskin, and B. J. Berne, J. Chem. Phys. **76**, 1347 (1982).
[23]B. J. Berne and D. Thirumali, Annu. Rev. Phys. **37**, 401 (1986).
[24]R. Hall and B. J. Berne, J. Chem. Phys. **81**, 3742 (1984).
[25]E. L. Pollock and D. M. Ceperley, Phys. Rev. B **30**, 2555 (1984).
[26]M. Sprik, M. L. Klein, and D. Chandler, Phys. Rev. B **32**, 545 (1985).
[27]M. Rao, C. Pangali, and B. J. Berne, Mol. Phys. **37**, 1773 (1979).
[28]P. J. Rossky, J. D. Doll, and H. L. Friedman, J. Chem. Phys. **69**, 4628 (1978).
[29]N. Metropolis, A. W. Rosenbluth, M. N. Rosenbluth, A. H. Teller, and E. Teller, J. Chem. Phys. **21**, 1087 (1953).
[30]J. A. Fleck, M. D. Feit, and A. Steiger, J. Comp. Phys. **47**, 412 (1982).
[31]J. D. Honeycutt and H. C. Anderson, J. Phys. Chem. **91**, 4950 (1987).